Space Weather

RESEARCH ARTICLE
10.1029/2018SW001932

Special Section:
Space Weather Events of 4-10 September 2017

The 6 September 2017 X-Class Solar Flares and Their Impacts on the Ionosphere, GNSS, and HF Radio Wave Propagation

Y. Yasyukevich[1], E. Astafyeva[2], A. Padokhin[3], V. Ivanova[1], S. Syrovatskii[1], and A. Podlesnyi[1]

[1]Institute of Solar-Terrestrial Physics SB RAS, Irkutsk, Russia, [2]Institut de Physique du Globe de Paris (IPGP), Paris Sorbonne Cité, University, Paris, France, [3]Faculty of Physics, Lomonosov Moscow State University, Moscow, Russia

Key Points:
- We investigated effects of the 6 September 2017 X-class solar flares on the ionosphere, GNSS-based navigation, and HF propagation
- The solar flares had a significant impact on the ionosphere, and the ionospheric effects lasted longer than the enhanced EUV emission
- The SRB associated with the X9.3 flare did not impact on the GNSS communication, but the X-ray emission caused blackout in HF propagation

Supporting Information:
- Supporting Information S1
- Animation S1
- Animation S2

Correspondence to:
E. Astafyeva,
astafyeva@ipgp.fr

Citation:
Yasyukevich, Y., Astafyeva, E., Padokhin, A., Ivanova, V., Syrovatskii, S., & Podlesnyi, A. (2018). The 6 September 2017 X-class solar flares and their impacts on the ionosphere, GNSS, and HF radio wave propagation. *Space Weather*, *16*, 1013–1027. https://doi.org/10.1029/2018SW001932

Received 1 MAY 2018
Accepted 4 JUL 2018
Accepted article online 13 JUL 2018
Published online 15 AUG 2018
Corrected 14 SEP 2018

This article was corrected on 14 SEP 2018. See the end of the full text for details.

Abstract On 6 September 2017, the Sun emitted two significant solar flares (SFs). The first SF, classified X2.2, peaked at 09:10 UT. The second one, X9.3, which is the most intensive SF in the current solar cycle, peaked at 12:02 UT and was accompanied by solar radio emission. In this work, we study ionospheric response to the two X-class SFs and their impact on the Global Navigation Satellite Systems and high-frequency (HF) propagation. In the ionospheric absolute vertical total electron content (TEC), the X2.2 SF caused an overall increase of 2–4 TECU on the dayside. The X9.3 SF produced a sudden increase of ~8–10 TECU at midlatitudes and of ~15–16 TECU enhancement at low latitudes. These vertical TEC enhancements lasted longer than the duration of the EUV emission. In TEC variations within 2–20 min range, the two SFs provoked sudden increases of ~0.2 TECU and 1.3 TECU. Variations in TEC from geostationary and GPS/GLONASS satellites show similar results with TEC derivative of ~1.3–1.7 TECU/min for X9.3 and 0.18–0.24 TECU/min for X2.2 in the subsolar region. Further, analysis of the impact of the two SFs on the Global Navigation Satellite Systems-based navigation showed that the SF did not cause losses-of-lock in the GPS, GLONASS, or Galileo systems, while the positioning error increased by ~3 times in GPS precise point positioning solution. The two X-class SFs had an impact on HF radio wave propagation causing blackouts at $<$30 MHz in the subsolar region and $<$15 MHz in the postmidday sector.

1. Introduction

Solar flares (SFs)—explosive events on the Sun—are undoubtedly the most intensive "disturbers" of the space weather. During SF, the Sun releases high-energy protons and electrons and intense radiation in all wavelengths that can affect not only the Earth's upper atmosphere but also propagation of radiowaves. The increased level of X-ray and of extreme ultraviolet (EUV) radiation results in ionization in the ionosphere on the sunlit side of the Earth (Liu et al., 2011; Mitra, 1974). Intense X-ray emission causes absorption in the lower ionospheric *D* layer, which results in degradation or complete absorption (i.e., radio blackout) of high-frequency (HF) signals. SFs are classified based on their peak emission in the 0.1–0.8 nm spectral band (i.e., X-ray) and are marked by letters "A," "B," "C," "M," and "X," identifying X-class flares as the most intensive ones with emission higher than 10^{-4} W m^{-2}.

Closely related to SF and quite threatening for the radio communication systems are solar radio emissions, or solar radio bursts (SRB). The intensity of SRB is measured in solar flux units (1 sfu = 10^{-22} W m^{-2} Hz^{-1}). SRB can be observed in a broad wavelength range from millimeter and centimeter wavelengths to meter and decameter wavelengths, originating from different altitudes of the solar atmosphere. SRB in the *L* band emission impact Global Navigation Satellite System (GNSS) communication and other radio systems through direct radio wave interferences (e.g., Afraimovich et al., 2007, 2008; Cerruti et al., 2006; Demyanov et al., 2013; Sreeja et al., 2014; Yue et al., 2013, 2018). SRB can cause reduction of signal-to-noise ratio and instantaneous or long-period losses-of-lock (LOL) of GNSS signals. Some failures in radio navigation parameters were recorded even when the solar radio flux power was as low as $4 \cdot 10^3$ sfu (Afraimovich, Demyanov, et al., 2008).

Solar EUV radiation has a decisive impact on the 120–200 km ionosphere, and a sudden increase of the EUV emission during SF causes an abrupt enhancement of the ionization that can last from minutes to hours. Therefore, study of the ionospheric response to SF has importance not only from the fundamental point of view but also for Space Weather applications. Ionospheric effects due to SF have been intensively studied for several decades. Recent development of ground-based networks of permanent GNSS receivers has opened a new means for observations of ionospheric response to SFs on a global scale (e.g., Afraimovich,

2000; Leonovich et al., 2002, 2010; Liu et al., 2004, 2007; Sripathi et al., 2013; Tsurutani et al., 2005, 2009; Yasyukevich et al., 2013; Zhang et al., 2011; Zhang & Xiao, 2005). Investigations of the ionospheric response to SFs suggest that their impact on the ionosphere varies from flare to flare. SF effects can be observed from predawn to postdusk regions, with most pronounced signatures in the noon region, where the solar zenith angle is close to zero (e.g., Leonovich et al., 2010; Liu et al., 2004, 2006; Xiong et al., 2014). Statistical analysis shows that the same X-class SFs near solar disccenter have much larger effect on the ionosphere than those near the solar limb regions (e.g., Le et al., 2013; Zhang et al., 2011). Le et al. (2013) also showed that larger ionospheric responses occur during equinoxes than during solstice periods, which can be explained by seasonal variation in the neutral density. In addition to that, Qian et al. (2011) showed that ionospheric and thermospheric effects of SFs depend on the rise rate and decay rate of SFs. However, despite numerous efforts, many features of the ionospheric response to SF are not properly understood yet and future studies are necessary.

The current 24th solar cycle began in December 2008 and is now decreasing in intensity and heading toward the solar minimum. However, despite the low solar activity period, a series of powerful SFs occurred in September 2017. In this paper, we focus on the X-class SFs of 6 September 2017, their ionospheric effects, and on their impact on the GNSS-based navigation and HF radio wave propagation.

2. Data and Methods

To study the 6 September 2017 SFs and to investigate their effects on the ionosphere, GNSS, and HF communication we analyzed the following sets of data:

A. X-ray 0.1–0.8 nm flux measured by GOES-13 (http://satdat.ngdc.noaa.gov/).
B. Solar radio emission from San Vito radiospectrograph of Radio Solar Telescope Network. We used spectrums in 18 to 180-MHz band and 1,415-MHz flux. A value of 1,415-MHz frequency is close to GPS/GLONASS operating frequency. (ftp://http://ftp.ngdc.noaa.gov/STP/space-weather/solar-data/solar-features/solar-radio/rstn-1-second/).
C. Fifteen-second SOHO/SEM EUV flux at 0.1–50 nm and at 26–34 nm. (https://dornsifecms.usc.edu/space-sciences-center/download-sem-data/; Space Sciences Center, University of Southern California).
D. Dual-frequency phase measurements by GNSS receivers. We used ~4,200 GNSS stations from the IGS (Dow et al., 2009), GHAIN (Jayachandran et al., 2009), TrigNet, GEOSCIENCE AUSTRALIA, CORS, LPIM, New Zealand (GEONET), Sonel, Unavco, KASI networks. Based on dual-frequency phase data we calculated the ionospheric total electron content (TEC; Hofmann-Wellenhof et al., 2008). To exclude TEC variations trend caused by satellite motion, we filtered data by using the running average with window 2–20 min. The variations are normalized on the satellite elevation using Klobuchar formula (Klobuchar, 1986). Further, to study the global distribution of TEC we calculated the integral TEC response on the dayside, as suggested by Afraimovich (2000). In addition to the GNSS-derived TEC, we analyzed the geostationary TEC estimations using Beidou-GEO signals (Kunitsyn et al., 2016) and variations of the absolute vertical TEC (VTEC). Data of the GPS-based VTEC with 5-min resolution are available from the Massachusetts Institute of Technology Haystack Observatory Madrigal database (Rideout & Coster, 2006; openmadrigal.org). To better understand the impact of the SF, we removed the quiet-time values from the disturbed ones, and we analyzed the resulting differential VTEC (dVTEC).
E. The SF impact on GNSS is estimated from the above data by analyzing the "quality" of the performance of GPS, GLONASS, and Galileo systems. The quality of GNSS performance was analyzed based on the following parameters:

1. Occurrence frequency, or the "density" of LOL (or phase slips), that is estimated as the total number of LOL divided by the total number of observations: $P = (N/S) * 100\%$. For the GPS/GLONASS, this parameter was estimated for L1 and L2 measurements, for Galileo—for L1 and L5 measurements.
2. Number of TEC slips, that is, errors in the TEC estimation. We considered a sudden jump of 1, 2, 3 TECU within 30-s to be a TEC slip at high, middle, and low-latitudes, respectively (Astafyeva et al., 2014).
3. Errors in the GNSS positioning. It is known that the accurate positioning is the primary task of the GNSS. However, it has been shown recently that the accuracy of positioning can degrade during geomagnetic storms, during observations of plasma bubbles, and during SRB (e.g., Afraimovich et al., 2013; Demyanov et al., 2012). We calculated the coordinates of GNSS stations in dual-frequency precise point

Table 1
M- and X-Class Solar Flares Occurred on 6 September 2017

Date	Class	Start (UT)	Max (UT)
06/09/2017	X2.2	08:57	09:10
06/09/2017	X9.3	11:53	12:02
06/09/2017	M2.5	15:51	15:56
06/09/2017	M1.4	19:21	19:30
06/09/2017	M1.2	23:33	23:39

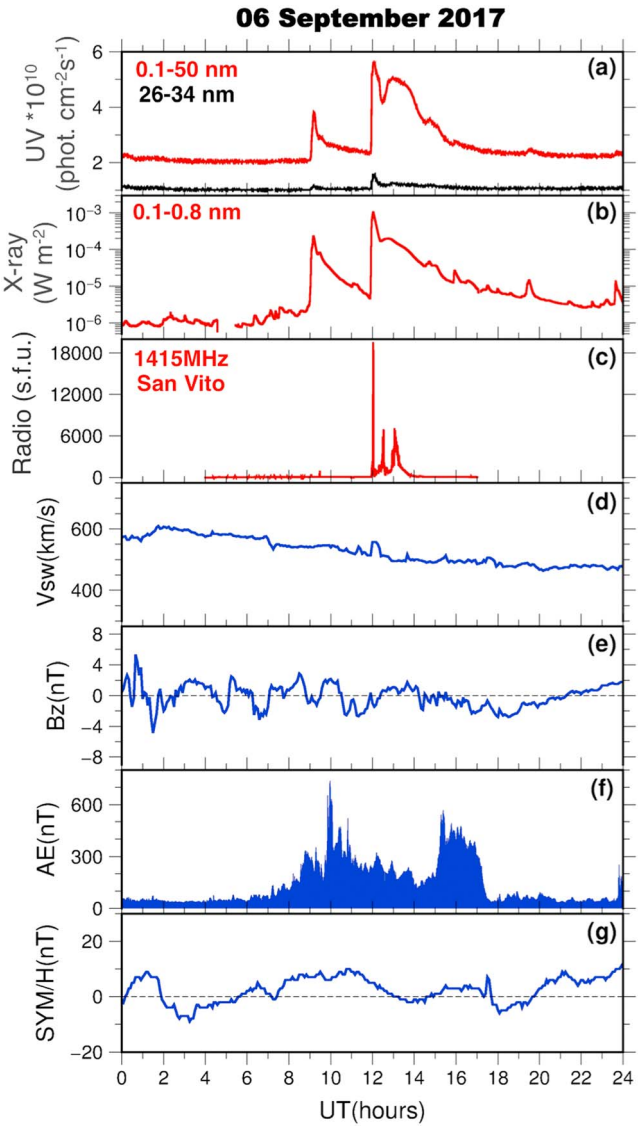

Figure 1. Variations in solar, interplanetary, and geophysical parameters on 6 September 2017: (a) 15-s average full solar disk EUV 0.1–50 nm (red) and 26–34 (black) nm flux from Solar and Heliospheric Observatory/solar EUV monitor; (b) X-ray irradiance in the range 0.1–0.8 nm as measured by GOES-13 satellite at 1 AU; (c) 1,415-MHz radio emission measured at San Vito Observatory (1 sfu = 10^{-22} W m^{-2} Hz^{-1}); (d) solar wind speed V_{sw}; (e) B_z component of the interplanetary magnetic field; (f) auroral electrojet index; (g) SYM/H index. Time resolution is 5 min for solar wind and geophysical parameters, 15 s for the UV, 2 s for the X-ray, and 1 s for the radio emission.

position mode (Zhou et al., 2018). We performed calculations for GPS and GLONASS separately. The median values of *X*, *Y*, *Z* coordinates during 24 hr are considered to be a true position. The error was calculated from the difference in the true and estimated coordinates as

$$\sigma = \sqrt{\Delta X^2 + \Delta Y^2 + \Delta Z^2} \quad (1)$$

F. Oblique-incidence HF-ionosonde sounding (OIS). Experimental network of ionospheric sounding is operated over the Siberian and Far Eastern regions of the Russian Federation. It is equipped with software-defined radio systems developed at the Institute of Solar-Terrestrial Physics (ISTP) SB RAS (Podlesny et al., 2011). The ISTP chirp ionosondes operate in the range of 4–30 MHz with the sweep rates of 500 kHz/s and radiated power of about 15 W. The interval between soundings is 5 min. The ISTP transmitters are located near Khabarovsk (47.6°N, 134.7°E), Magadan (60°N, 150.7°E), and Norilsk (69.2°N, 88°E), while the receiver is located near settlement Tory (51.8°N, 103°E), Buryatia (Figure 12). The Cyprus transmitter (35°N, 34°E) is equipped by the chirp sounder with the sweep rate of 100 kHz/s, the frequency range of 8–32 MHz (Vertogradov et al., 2017), and intervals between soundings of 15 min. The path lengths are 3,100, 2,300, 2,200, and 5,700 km for Magadan-Tory, Khabarovsk-Tory, Norilsk-Tory, and Cyprus-Tory paths, respectively.

The OIS data represent a set of ionograms. Each ionogram is a three-column array where the frequencies, group paths, and normalized amplitudes for the received HF signals are recorded. In this study we used the lowest observed frequency (LOF) values, that is, the smallest frequencies at the distance-frequency characteristics when the useful signal is observed. Besides that we used the summation of normalized amplitudes by the whole ionogram as a qualitative index of HF signals energetic characteristics.

3. Solar Flares of 6 September 2017 and Geomagnetic Conditions

On 6 September 2017 the Sun emitted several M-class flares and two X-class flares (Table 1). The first X-class flare of X2.2 peaked at 09:10 UT, and the second one of X9.3 peaked at 12:02 UT (Figures 1a–1c). The latter flare was the largest in the current 24th solar cycle and caused HF radio emission that lasted for ~1.5 hr (Figure 1c). The maximum of SRB was recorded at 12:00–12:10 UT. The UV flux increased up to 4 * 10^{10} (phot. cm^{-2} s^{-1}) during the X2.2 flare and up to 5.8 * 10^{10} (phot. cm^{-2} s^{-1}) during the X9.3 flare. The UV emission diminished shortly after the peak of the X2.2 flare, while after the X9.3 flare the intense UV flux was recorded during much longer time (Figure 1a). Shortly after the flare onset, the UV first diminished but then increased again up to 5.0 * 10^{10} (phot. cm^{-2} s^{-1}) and remained increased for ~2.5–3 hr.

During the day of 6 September 2017, the level of geomagnetic activity remained low (Figures 1d–1g). The solar wind speed varied between 480 and 600 km/s, and no step-like changes were recorded (Figure 1d). The maximum changes of ±6 nT of the Interplanetary Magnetic Field B_z component were registered from 0 to 2 UT on 6 September 2017 (Figure 1e). The auroral electrojet index rose several times during the day but did not exceed 700 nT (Figure 1f). The high-resolution global

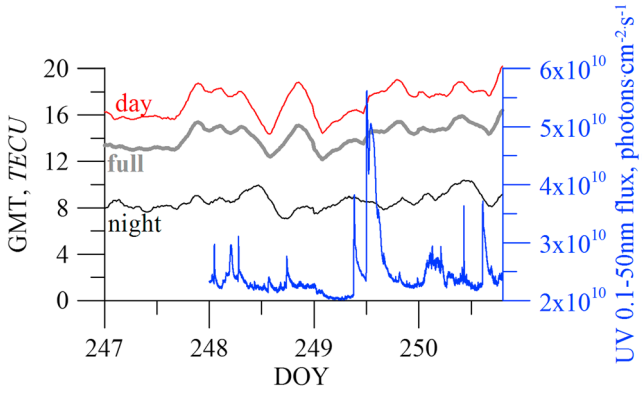

Figure 2. Dynamics of the global mean total electron content on the dayside (red line), nightside (black line), and in total (thick gray line) during 247–250 days of year (4–7 September 2017). The blue curve shows the Solar and Heliospheric Observatory/solar EUV monitor UV 0.1–50 nm flux.

storm index SYM/H did not show drastic changes either: It varied from −6 to +10 nT (Figure 1g).

4. Results and Discussions

4.1. Ionospheric Response to the X-Class Solar Flares of 6 September 2017

To understand the effects of the 6 September 2017 SFs on the ionosphere, it is of interest to first estimate their global contribution. For this purpose, we analyze the Global mean TEC (GMT; Hocke, 2008; Liu et al., 2009) which is similar to the global electron content concept that was first proposed by Afraimovich, Astafyeva, et al. (2008). In this work the GMT is calculated from the UPCG (UPC-IonSAT) global ionosphere maps with 15-min time resolution (e.g., Schaer, 1998). The GMT equals to the total number of electrons in the Earth ionosphere, normalized on the surface area. Therefore, the GMT is the weighted mean TEC from the global ionosphere maps. The GMT variations for 4 days around the SF day are shown in Figure 2. One can see that the X2.2 flare did not seem to cause any effect on the GMT, while the X9.3 flare that was accompanied by a prolonged intensification of the UV emission provoked ~2 TECU sudden rise in the dayside GMT (Figure 2, red curve), which is about 1 TECU increase in the full GMT (Figure 2, gray curve).

To study the ionospheric response to the 6 September 2017 SFs in more details, we analyze variations of the absolute VTEC (data from the Madridal Web services, as mentioned above) and of the dVTEC as compared to

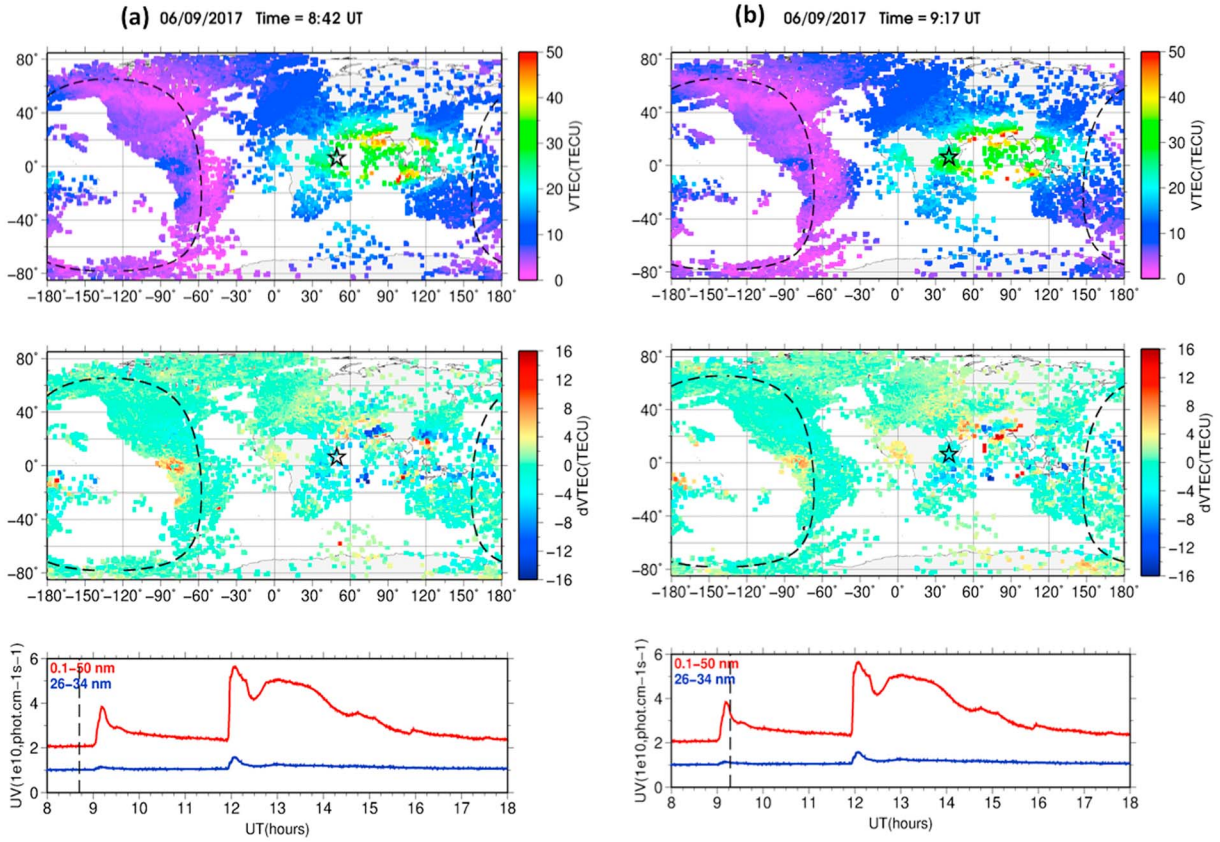

Figure 3. Maps of the (top) absolute vertical total electron content (VTEC), (middle) absolute differential VTEC several minutes (a) before and (b) during the maximum of the X2.2 flare of 6 September 2017. The corresponding color scale is shown on the right of each panel. The black star shows the position of the subsolar point, and the dotted curves indicate the positions of the sunrise and sunset solar terminator at the altitude of 300 km. (bottom) EUV variations from 8 to 18 UT with vertical dotted line marking the current moment of time (UT) and the EUV value. Time in UT is also shown on the top of the panels.

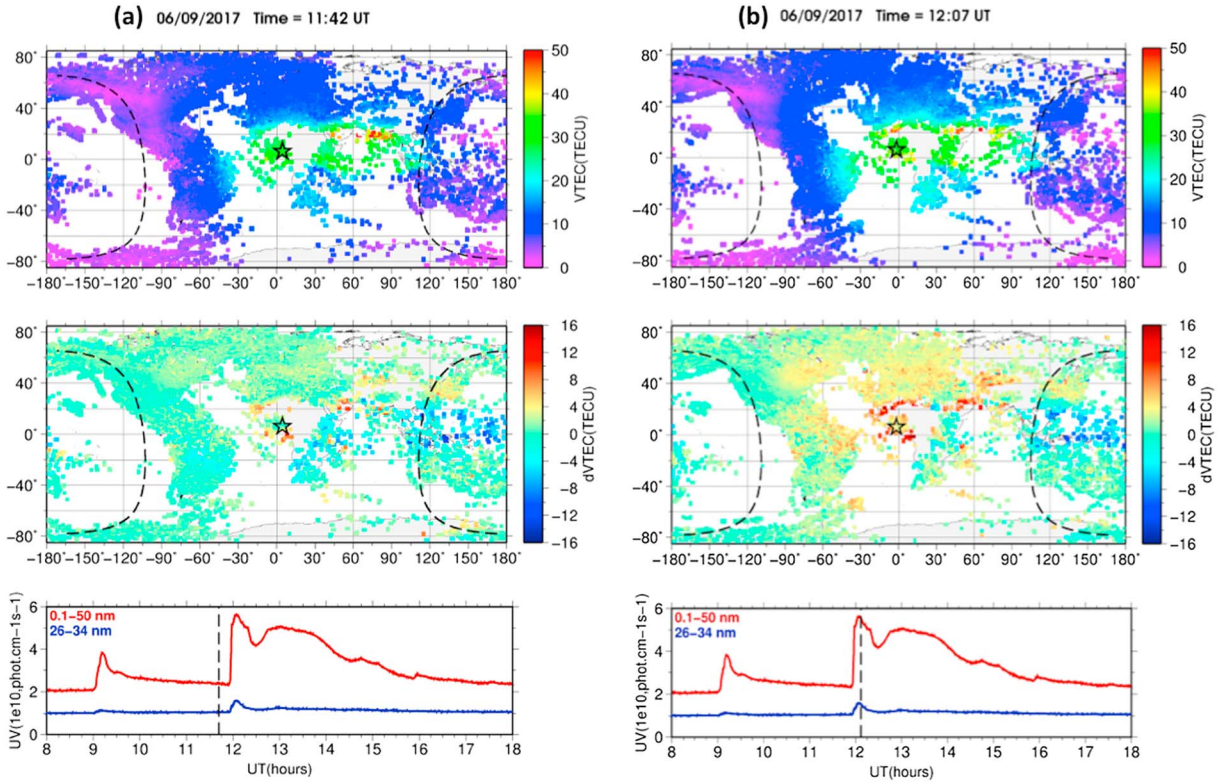

Figure 4. Same as Figure 3 but (a) before and (b) during the X9.3 flare of 6 September 2017.

the quiet-time VTEC level. As the reference value, we take the averaged VTEC for two quiet days, 4 and 5 September 2017.

The VTEC and dVTEC before and during the X2.2 and X9.3 flares are shown in Animation S1 in the supporting information and in Figures 3 and 4. One can see that before the flares, the absolute VTEC varied within 2–10 TECU on the nightside and within 10–50 TECU on the dayside, reaching 45–50 TECU within the area of the equatorial ionization anomaly (EIA) in the afternoon sector (Figure 3a and Animation S1). At midlatitudes, the preflare dayside VTEC reached 20–30 TECU. In the dVTEC, we observe strong negative deviations from the quiet day of $-12 \div -16$ TECU in the EIA area due to natural day-to-day variability. At midlatitudes, the dayside preflare dVTEC does not exceed ±4–6 TECU in both hemispheres. The beginning of the X2.2 flare at 8:57 UT cannot be seen clearly in the absolute VTEC, while in the dVTEC one can observe an overall increase of ~3–4 TECU at middle and low latitudes around the subsolar point. We note that this increase seems to be more pronounced in the northern hemisphere (NH) than in southern hemisphere (SH). The dVTEC in the NH remained increased until the beginning of the second flare.

The X9.3 flare caused more pronounced effect of the ionospheric VTEC. The onset of the second X-class flare at 11:53 UT (11.88 UT) caused an immediate increase of VTEC on the whole dayside, with the maximum enhancement around the subsolar point. This increase is seen in both VTEC and dVTEC. At ~12:02–12:12 UT the absolute dVTEC showed a deviation of ~8–10 TECU at middle latitudes and up to 12–16 TECU at low latitudes (Figure 4 and Animation S1). This enhancement concerned, first of all, European and African regions but also western part of Asia and eastern part of the American sector. The observed VTEC increase appeared to be stronger in the NH, but it can also be a seeming effect because of fewer observations in the SH. Further, following the fast decay of the EUV emission, the flare-related enhancement slightly diminished by 12:18–12:30 UT (Animation S1, bottom panel). From ~12:36 UT, the EUV flux increased again and caused an enhancement in the dayside VTEC and dVTEC at equatorial and midlatitudes (Animation S1). This second increase in the EUV emission lasted until ~14 UT, and then gradually decayed. Animation S1 demonstrates that during this period of time the VTEC remained enhanced throughout the

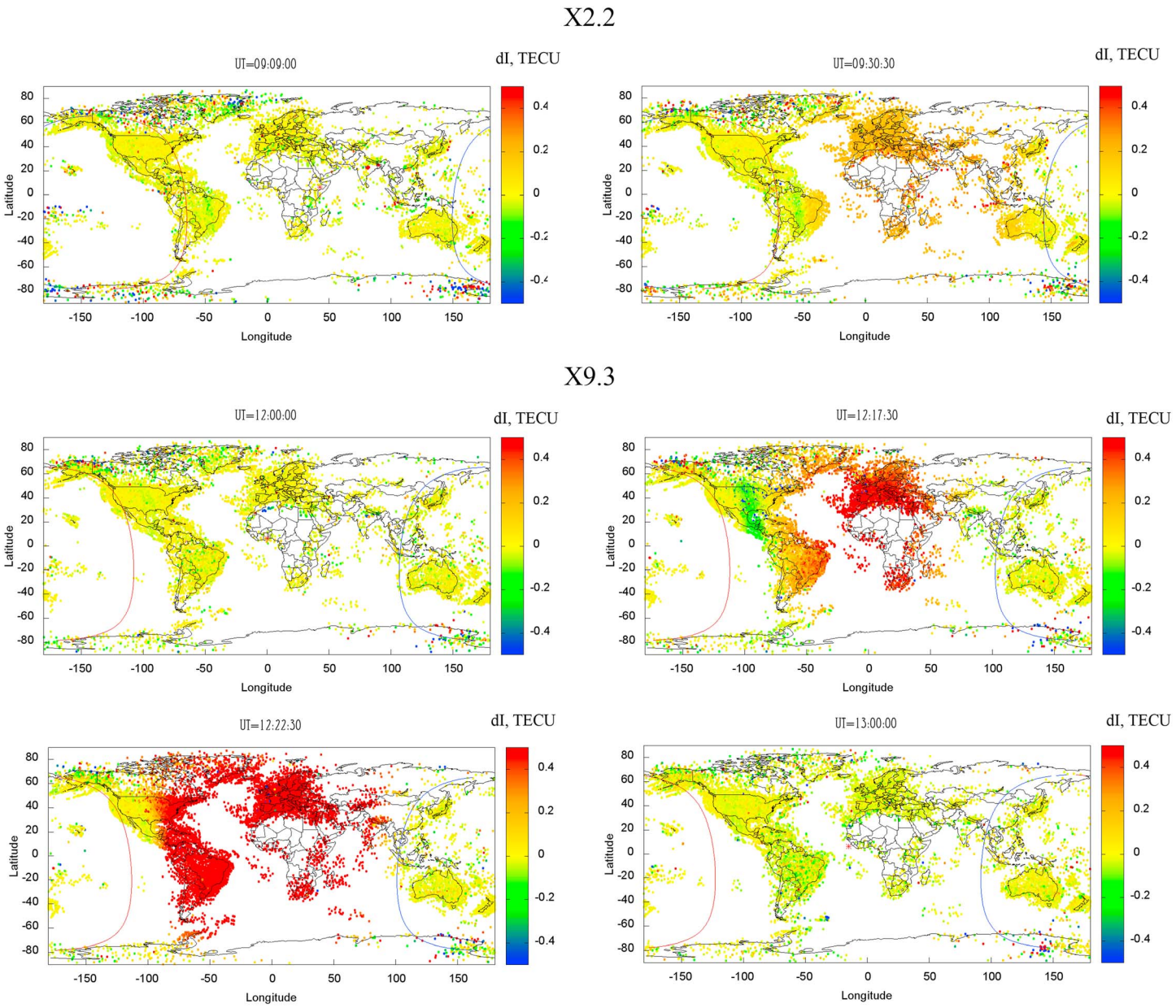

Figure 5. Maps of TEC variations filtered within 2–20 min range. The corresponding color scales are shown on the right of each panel. The red and blue lines show the sunrise and sunset solar terminator at 300 km, respectively. (top row) Results for the X2.2 flare (for 09:09:00 UT and for 09:30:00 UT) and (middle and bottom rows) the results for the X9.2 flare (moments of time as indicated: 12:09:00 UT, 12:17:30 UT, 12:22:30 UT, 13:00:00 UT).

dayside. The most significant dVTEC increase of ~16 TECU can be observed at ~14:12–14:54 UT in the EIA region over the east coast of South America, when the subsolar point moved closer to the American region. During this period of time, the EIA seemed to be reinforced during the SF, which is contrary to previous results showing the EIA depression during SFs (e.g., Liu et al., 2007; Zhang et al., 2017). We also notice that the observed dVTEC enhancement appeared to be stronger in SH.

The low-latitude dVTEC enhancement started to diminish with the decay of the EUV emission intensity and with further westward displacement of the subsolar point, however, the dVTEC remained increased until ~17:30 UT. At midlatitudes of NH, ~4–8 TECU dVTEC enhancements can be observed through the entire SF duration and until ~17:18 UT. Therefore, at both low and midlatitudes we notice several hours of delay between the decay of the EUV emission and the VTEC decrease. Such long VTEC "recovery" can be

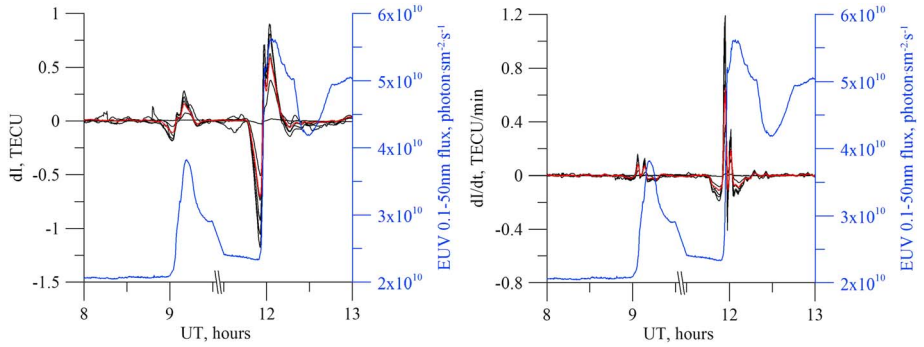

Figure 6. (left) Mean total electron content (TEC) 2–20 min variation value and (right) mean time derivative of TEC. Dynamics for whole dayside is shown in red. In black we shown dynamics for different Sun elevations with 20° step. The blue line shows EUV flux at 0.1–50 nm.

explained by rather long decay of the flare emission (as shown by Qian et al., 2011) and/or by large contributions from higher altitudes (above 300 km) where the recombination is lower (Le et al., 2016). In addition, coupling between the ionosphere and the thermosphere which is also largely perturbed by SF can play a role. A hemispheric asymmetry in the ionospheric response to SF is often attributed to seasonal thermospheric effects and to related changes in the neutral composition (Tsugawa et al., 2006). Besides the thermosphere, the asymmetry can be introduced by electrodynamical changes caused by SF (Zhang et al., 2017).

In addition to the absolute VTEC, we also analyze TEC variation data (dTEC). This kind of data allows excluding the effects of regular ionosphere. To create the dTEC maps, we used data from ~4,200 receivers of permanent global and regional GNSS networks. Figure 5 shows 2–20 min dTEC maps for several moments of time on 6 September 2017. The full dynamics of the dTEC for the period of time from 8 to 18 UT can be found in Animation S2 (available as the supplementary materials). Figure 5 and Animation S2 show that for both SF we observe dTEC enhancement at all latitudes on the dayside. The maximum value of ~0.5 TECU is observed around the subsolar points, while smaller response can be seen at the regions close to the solar terminator. During the X2.2 SF the main effects are seen over Europe, while the unlit American ionosphere demonstrates almost no effect. During the X9.3 SF the subsolar point shifts to the European and Atlantic regions, and the effects are quite significant in the American sector as well.

To understand the overall effect we calculated the integrated response at different Sun elevations (similar to Yasyukevich et al., 2013). At each station we calculate raws of TEC and the corresponding ionospheric pierce points (IPP). Then we make TEC running average filtering and delete the trend with different windows (Afraimovich et al., 2013) and calculated the time derivative of TEC. For each IPP we calculated the solar elevation and the corresponding mean TEC variation and the mean time derivative of TEC.

The dynamics of the integrated mean TEC variation value and mean time derivative of TEC are shown in Figure 6. Dynamics for the whole dayside is shown in red. In black we show dynamics for different Sun

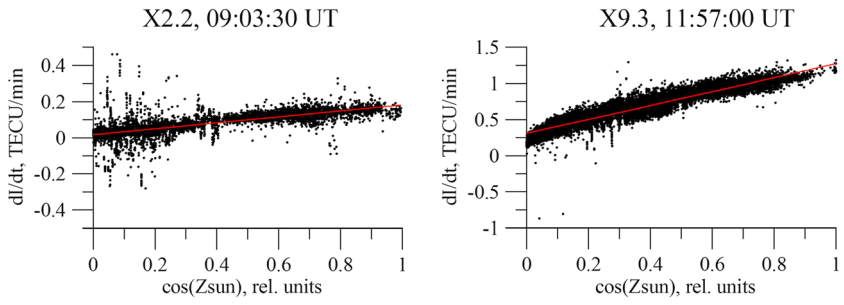

Figure 7. Dependence of the total electron content derivative on the solar zenith angle. The red line shows the linear approximation.

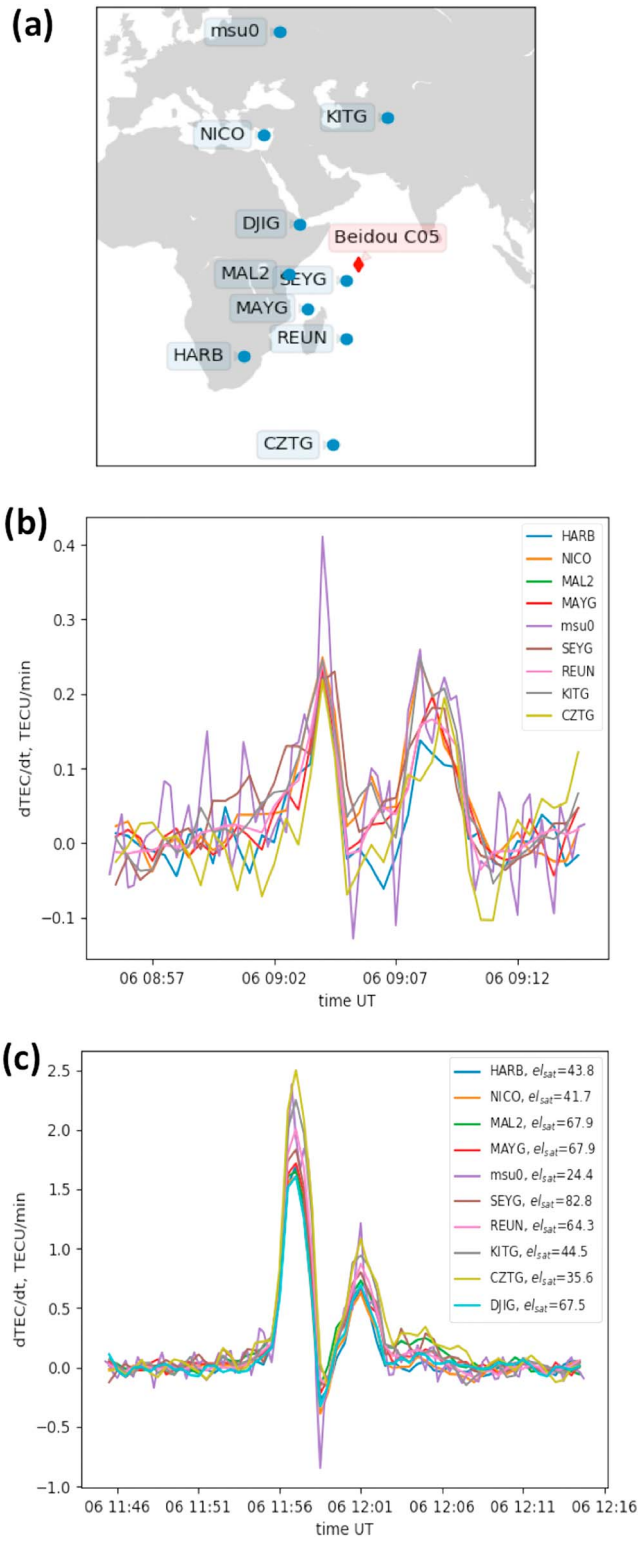

Figure 8. Dynamics of vertical total electron content derivative from the Beidou adjusted to the solar zenith angle for (b) X2.2 and (c) X9.3 solar flares of 6 September 2017. (a) Positions of the receivers. The red diamond corresponds to the position of the Beidou C05 satellite.

elevations with 20° step. The negative response is connected with the filter effect. The filtering results in zero mean value, so any increase will be shown as decrease with the minimum on the event onset. The mean magnitude (difference from maximum to minimum) of TEC variations on the whole sunlit area was ~1.3 TECU for X9.3, and ~0.2 TECU for X2.2. The maximum magnitudes were recorded at subsolar regions. Their mean values were 2.1 TECU and 0.45 TECU for X9.3 and X2.2, correspondingly. The maximums of TEC variations correspond to the maximums in the UV emission. The differences in the TEC rate for the two considered flares are more significant than those in TEC variations. TEC derivative shows several peaks that coincide with the maximums in the UV flux rate. The mean value of the maximum TEC rate is 0.557 TECU/min for X9.3 and 0.071 TECU/min for X2.2.

To further evaluate the effect of the flares on the dayside, we estimate dependence on solar zenith angle (Zsun). Wan et al. (2005) showed that the time rate of the flare-induced TEC increment is proportional to the effective flare radiation flux; thus, TEC derivative should be proportional to cosine of the solar zenith angle. Figure 7 shows the TEC derivative for the two timestamps corresponding to the X2.2 (left) and X9.3 (right) SFs. The timestamps correspond to the maximum values of the TEC derivative (Figure 6). Both flares show almost linear dependence on cos(Zsun). The relative noise level for the X2.2 SF seems to be higher than that for the X9.3 SF. It is possibly caused by lower energy which is not enough to overcome local processes. Linear regression allows us to obtain dependence of SF response at different solar zenith angles:

$$\text{X9.3}: \mathrm{dI/dtmax} = 0.959\ \cos(\mathrm{Zsun}) + 0.311\ [\mathrm{TECU/\,min}].$$

$$\text{X2.2}: \mathrm{dI/dtmax} = 0.165\ \cos(\mathrm{Zsun}) + 0.017\ [\mathrm{TECU/\,min}].$$

It should be noted that estimation of the dTEC by using the GNSS has several disadvantages. One of them is a change in the line-of-sight which influences the obtained data. Kunitsyn et al. (2015,2016) suggested TEC estimations using geostationary Beidou and SBAS satellites which have the advantage of virtually static IPPs. In that case no special filtering procedure is required to account for satellite motion, as it is in GPS/GLONASS case, and TEC derivative during an SF event can be estimated directly without filtering artifacts. Note that such estimations are beneficial for the equatorial region where geostationary satellites have the highest elevations, while for midlatitude stations satellite elevations are pretty low, so that the obtained results may significantly suffer from the horizontal gradients of the electron density.

For the current study we have chosen 10 GNSS stations (9 IGS stations and 1 self-operated MSU0 station) in Europe-Africa that capture geostationary Beidou (BDS) signals. Their locations are shown in Figure 8a. Note that we consider both near-equatorial and midlatitude stations. For all those stations we estimate geostationary relative slant TEC using signals of BDS C05 satellite (marked as red diamond in Figure 8a), which has the highest elevation for that region among all geostationary BDS satellites in the constellation. For both X-class events of 6 September 2017 we compute slant TEC derivatives, apply simple geometric oblique factor, and adjust the results for the solar zenith angle at IPPs. We also account for undisturbed TEC behavior using polynomial fit to the data before and after the flare. The results are presented in Figures 8b and 8c. Among

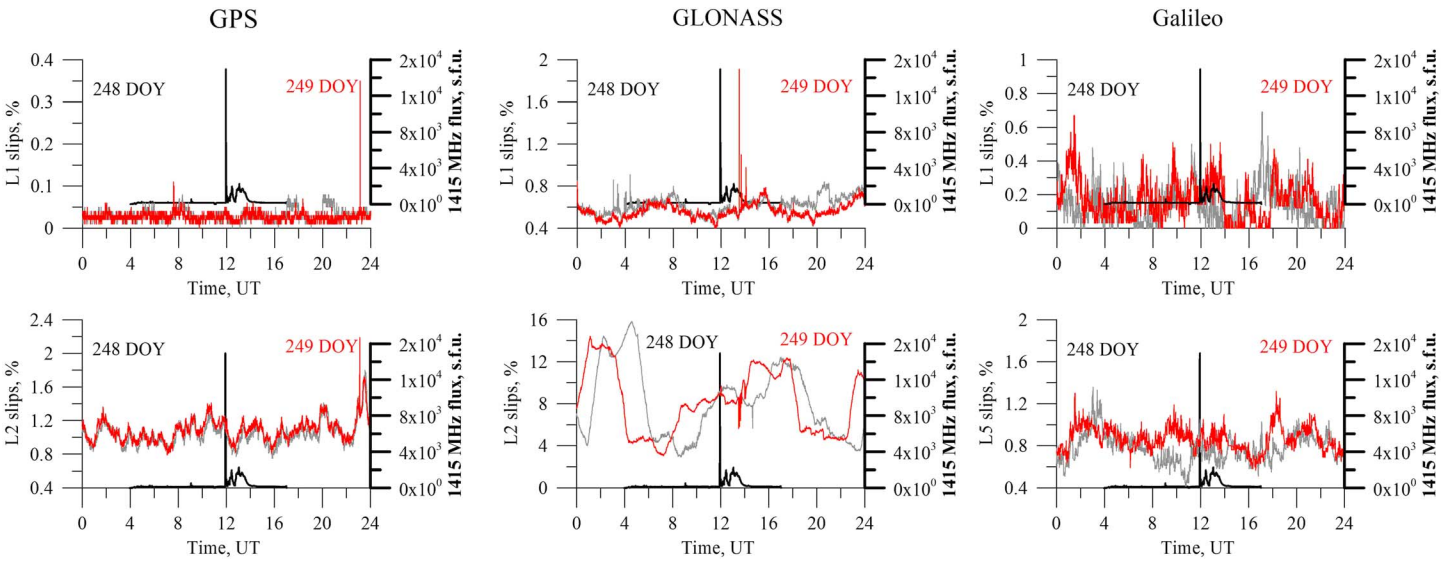

Figure 9. Dynamics of losses-of-lock for (left column) GPS, (middle column) GLONASS, (right column) Galileo signals. (top row) L1 and (bottom row) L2 (GPS/GLONASS) and L5 (Galileo). Losses-of-lock on 6 September (DOY249) are shown in red, on 5 September (DOY248) are in gray. The black thin curve shows the 1,415-MHz flux from San Vito radio observatory (right axis).

local TEC variations, coherent response of TEC derivative to both SFs is clearly observed. Note that the maximum values of the observed flare induced TEC derivatives vary significantly from station to station even after the correction for oblique factor and solar elevation. For MSU0 station this result can be to some extent explained by higher sampling of the data (15 s as compared to 30s for all other stations). Closer look at the Figure 8 shows that the most outfitted TEC derivative values are observed for the stations with the lowest elevation angles of Beidou C05 satellite (such as once again MSU0, CZTG, and KITG). It suggests that simple slant TEC to VTEC conversion based on common used geometrical oblique factor (Schaer et al., 1998) applied here is not accurate enough for those sites due to the presence of significant horizontal gradients of electron density.

To get more reliable TEC derivative estimates one should consider stations with highest possible geostationary satellite elevation, such as SEYG. For that station we get ~0.24 TECU/min for X2.2 event and ~1.7 TECU/min for X9.3 event, which is in line with GPS/GLONASS data. The TEC derivative from GPS/GLONASS data are smaller than those from BDS geostationary data, which is most likely due to 2-min cutoff in the filter used for GPS/GLONASS data, while some SF energy released in the variations with time scales less than 2 min. Another factor is that with geostationary satellites one effectively estimates TEC up to geostationary orbit height which is ~16,000 km higher than those for GPS/GLONASS. Nevertheless, taking into account the characteristic times for ionization reactions in the plasmasphere, that impact can be considered negligible compared to the filtering effects.

4.2. Performance of the GNSS During the X-Class Solar Flares of 6 September 2017

One of the most important parameters in GNSS operation "quality" is level of LOL. In this work, we analyzed the dynamics of LOL at L1 and L2 frequencies for GPS and GLONASS, and for L1 and L5 signals for Galileo. Figure 9 shows no significant increase in the LOL occurrence frequency corresponding to the SRB of 6 September 2017, which is a surprising result. As shown by Afraimovich, Demyanov, et al. (2008) and Demyanov et al. (2013), strong solar radio emission can increase loss-of-lock density due to the increase in noise level at the receiver input. Afraimovich, Demyanov, et al. (2008) showed that even 4,000–12,000 sfu can be a threat to GNSS stability. During the X9.3 SF the maximal flux at 1,415 MHz (i.e., close to the GNSS operating frequencies) reached 19,604 sfu, but we do not observe any effect in GPS, GLONASS, or Galileo data.

It should be noted that in previous works LOL were mainly recorded at L2 frequency, while L1 measurements were usually reported to be stable; such an effect was explained by stronger signal power at L1 than at L2 during previous years. Now, the observed low level of LOL during the September 2017 high-intensity SRB

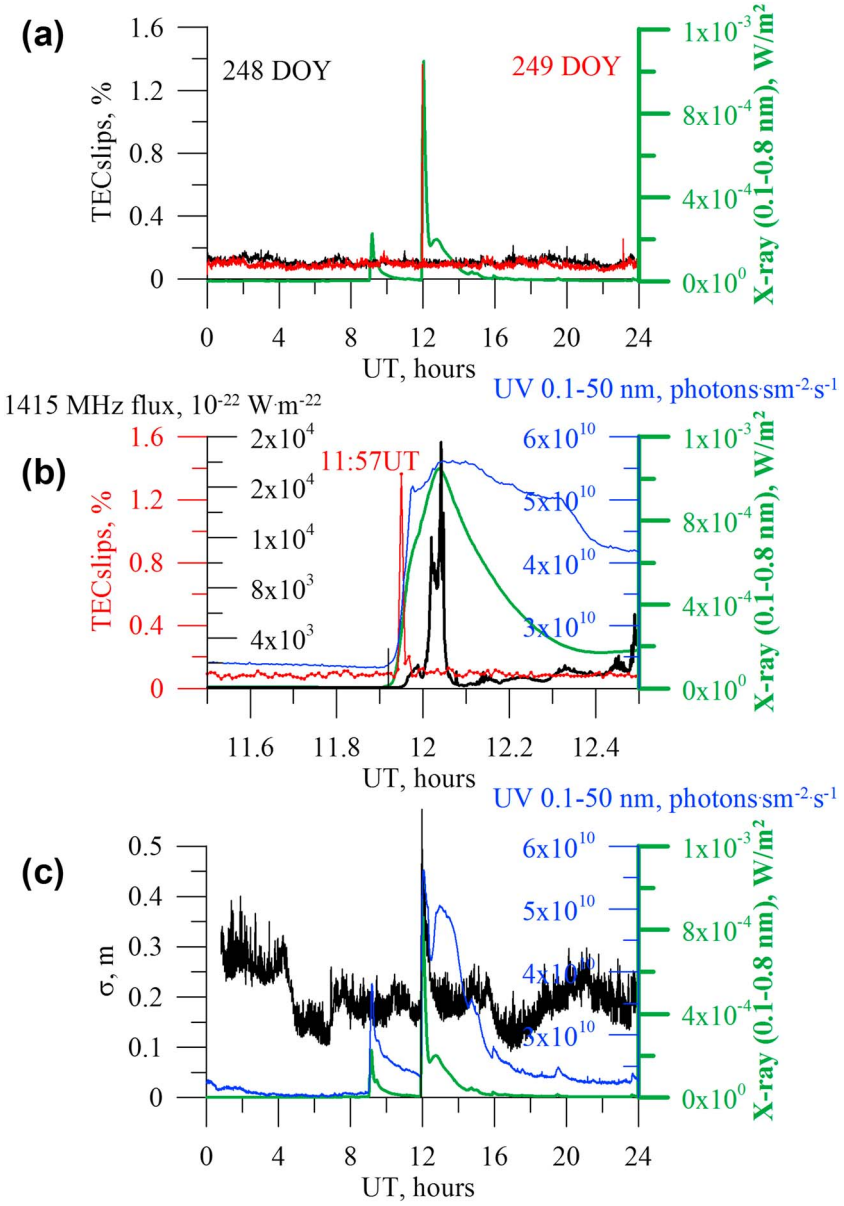

Figure 10. (a) Dynamics of the total electron content (TEC) slips on 5 September 2017 (black) and 6 September 2017 (red); (b) variations of TEC slips (red), Solar and Heliospheric Observatory (SOHO)/solar EUV monitor (SEM) UV 0.1–50 nm flux (blue), GOES-13 X-ray 0.1–0.8 nm flux (green), and 1,415-MHz flux (black) during the X9.3 flare on 6 September 2017; (c) GPS precise point position error (black), SOHO/SEM UV 0.1–50 nm flux (blue), and GOES-13 X-ray 0.1–0.8 nm flux (green) during the day of 6 September 2017.

could be explained by an increased signal power at L2 channel as compared to previous years. Indeed, according to GPS interface control document the power of L2 transmitter has been increased by ~3–5 dBw (IRN-IS-GPS-200H-003, 2016). On the receivers' side, we also find an increase of signal-to-noise ratio (S2) at L2 of several GPS satellites (not shown as a figure).

Another parameter that can show the degradation in GNSS operation is the rate of TEC slips (Afraimovich et al., 2013; Astafyeva et al., 2014). Zakharov et al. (2016) suggested that TEC slips occur due to problems in phase determination. Astafyeva et al. (2014) showed that the occurrence of the TEC slips significantly depends on latitudes. Kozyreva et al. (2017) demonstrated that for the 5 April 2010 magnetic storm ~70% of TEC slips occur within the auroral oval region, while the others occur in the vicinity of its equatorward boundary. All these research teams showed high TEC slips sensitivity to space weather events.

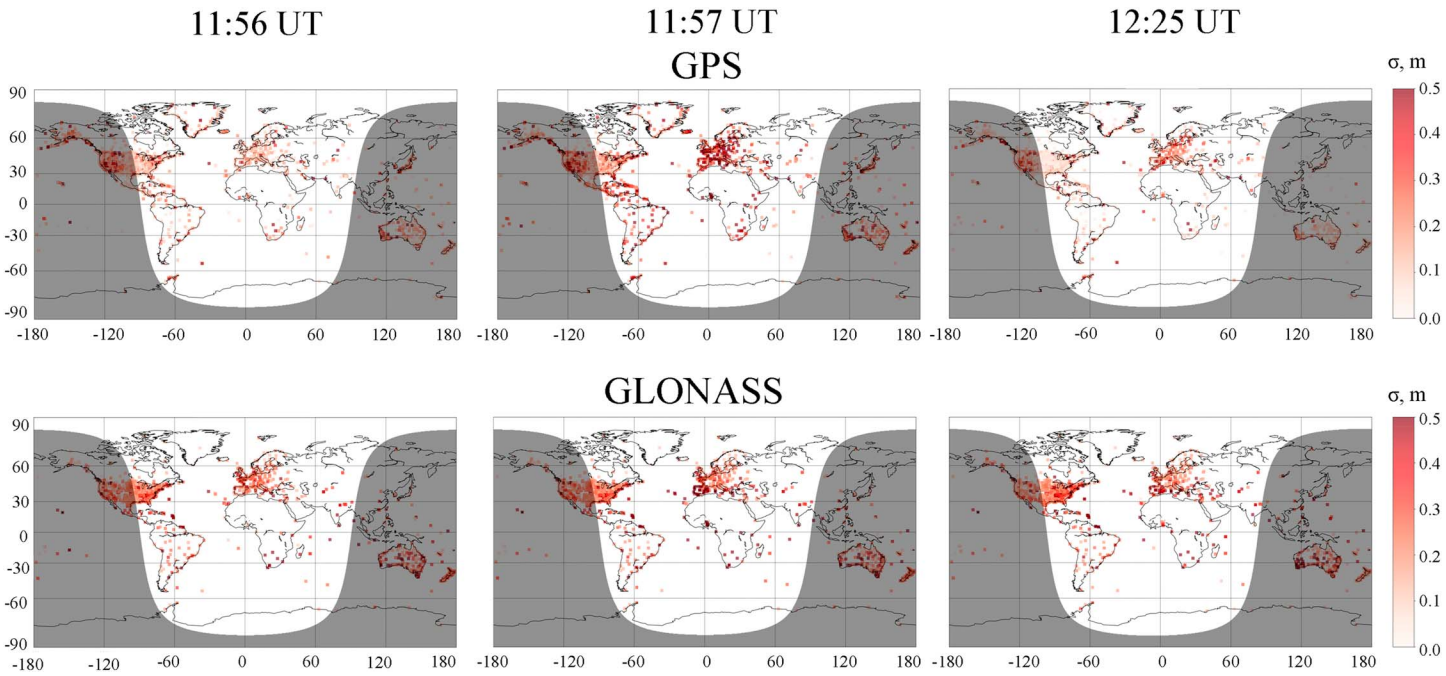

Figure 11. (top row) GPS and (bottom row) GLONASS precise point position errors at different stations before the X9.3 flare at (left column) 11:56 UT and after the solar flares onset at (medium column) 11:57 UT and at (right column) 12:25 UT.

The results for TEC slips are shown in Figures 10a and 10b. One can see a sharp short-term burst in TEC slips at ~12 UT on 6 September 2017 (Figure 10a). This TEC slip burst reached 1.36%, which is lower than during superstorms (Astafyeva et al., 2014). Closer look at the TEC slip behavior with respect to solar parameters indicates that the observed peak in TEC slips was not related to the SRB but occurred with the SF onset at 11:57 UT. It should be noted that the observed peak in the TEC slip ratio was most likely caused by the sudden increase in the TEC due to the abrupt increase in the solar UV emission, and not by the SRB. As mentioned in section 2, we defined a sudden jump of 1, 2, 3 TECU within 30 s at high, middle, and low latitudes, respectively, as a TEC slip. Figure 7 shows that the mean derivative for the VTEC does not exceed 1.5 TECU/min; however, at low elevations the TEC derivative in the equatorial area could exceed 3 TECU/30 s. Consequently, at low latitudes the TEC derivative could exceed the selected thresholds for the TEC slips. In the subsolar sector (Africa), we have only a few GNSS stations, but the overall rate of the TEC slips reached 1.3%. This all might signify that the observed effect is not just a TEC increase but is an effect of the increased solar emission.

In addition to the LOL and TEC slips we also analyzed the positioning error. Figure 10c shows the dynamics of the GPS PPP errors averaged over the area of (−30:30°N, −30:60°E) on 6 September 2017. One can see that after the beginning of the X9.3 flare the GPS PPP error increased from ~0.15–0.2 m to ~0.57 m. Such dynamics of GPS PPP error correlates with the increase in the X-ray flux.

Figure 11 shows the global distribution of positioning error σ during the X9.3 flare. One can see that during the SF the positioning error increased for both GPS and GLONASS systems. Such an effect is observed on the sunlit part of the Earth: on the major part of Africa and Europe, and also (but less pronounced) in South and North America. At 11:56 UT, before the flare, the mean PPP errors over the area of (−30:30°N, −30:60°E) were ~0.17 and ~0.47 m for GPS and GLONASS, respectively. These values sharply increased up to 0.46 and 0.56 m after the SF onset. Such worsening of the positioning lasted for ~30 min until ~12:25 UT. The averaged PPP errors during this period of time over the area of (−30:30°N, −30:60°E) reached ~0.57 and ~0.56 m, for GPS and GLONASS. Overall, our results show that the positioning quality for GPS decreased by ~3 times during the flare. However, it should be noted that the background level of PPP errors in GLONASS is relatively high, and the effect of SF is not well seen.

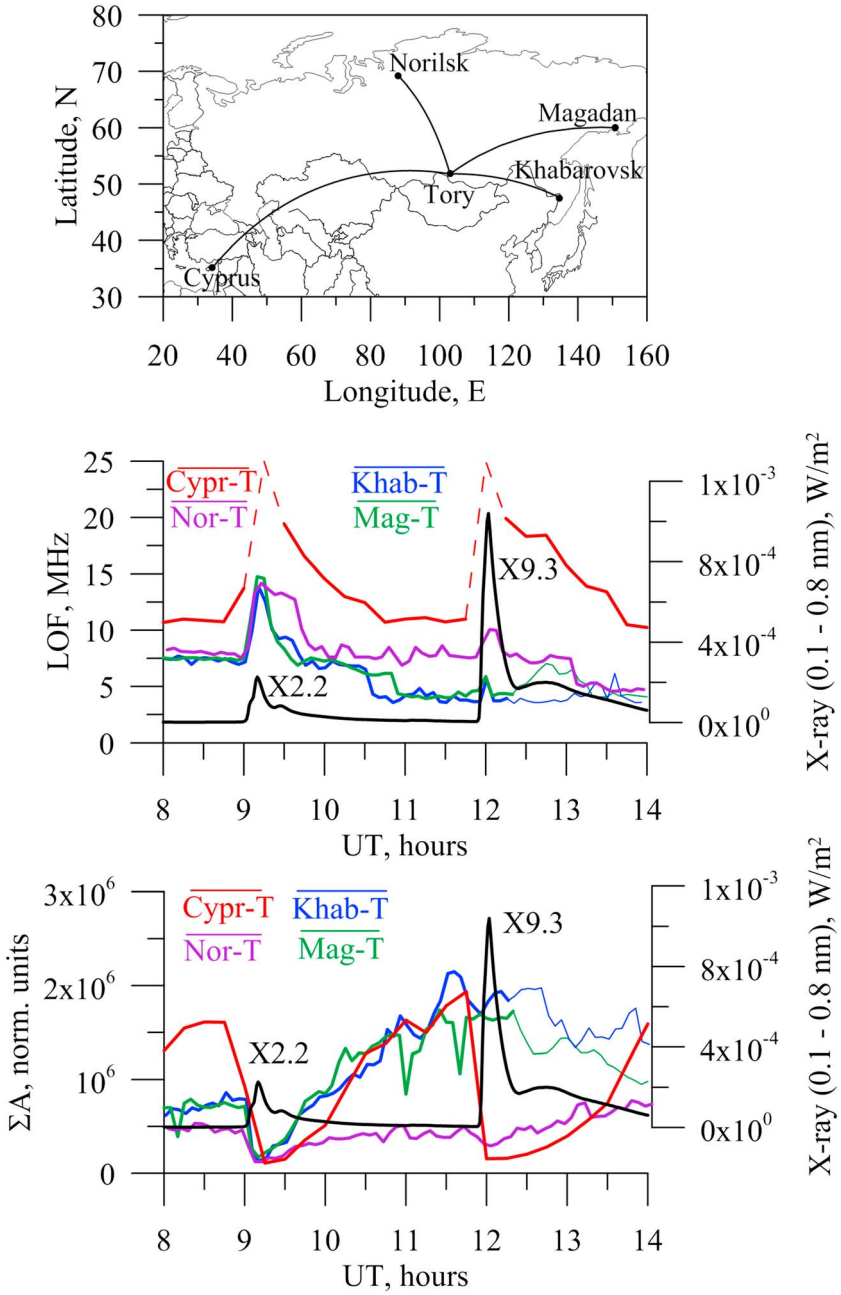

Figure 12. High-frequency communication signals on 6 September 2017. (top) Positions of transmitters (Norilsk = Nor, Magadan = Mag, Cyprus = Cypr) and a receiver (Tory = T). (middle) Lowest observed frequency. (bottom) Summarized signal amplitude. The bold colored lines show data for sunlit midpoints. Legends are on the panels. The black curve shows GOES-13 X-ray flux, and the corresponding Y-scale is shown on the right.

Less intensive X2.2 SF did not result in significant worsening of the positioning quality of GPS and GLONASS systems.

4.3. HF Radio Propagation During the 6 September 2017 X-Class Solar Flares

Solar flares can significantly impact on radio communication, especially on high frequency systems. The main peculiarity of SF influences to the HF propagation is the increase in decameter wave absorption in the ionospheric *D* layer (Zaalov et al., 2015). Bursts of X-ray flux during SF cause significant increase in *D* layer

ionization in the sunlit ionosphere. That results in considerable attenuation of HF signals during X-ray SF (Berngardt et al., 2018).

For the two X-class SFs of 6 September 2017 we analyze the HF propagation data obtained from four OIS sounding paths (Figure 12, upper panel). Three transmitters were located over northeastern regions of Eurasia (next to Khabarovsk, Magadan, and Norilsk), and one of those was located over the central Eurasian part (Cyprus). Khabarovsk-Tory, Magadan-Tory, and Norilsk-Tory paths are one-hop ones, while Cyprus-Tory path is two-hop one. During the X2.2 SF on 6 September 2017 all studied OIS paths were located at the sunlit ionospheric regions. During the X9.3 SF Cyprus-Tory and Norilsk-Tory paths were located at the sunlit parts of the Earth, while Khabarovsk-Tory and Magadan-Tory paths were in the nightside region.

Figure 12 (middle) shows LOF variations over the studied paths for 6 September 2017. During the X2.2 SF with the maximum X-ray value at 09:10 UT, LOFs increase sharply over all investigated paths. Full absorption of HF useful signal is observed over Cyprus-Tory path at 09:15 UT. Blackouts are shown schematically by the dashed lines. For Norilsk-Tory, Khabarovsk-Tory, and Magadan-Tory paths LOF grew by 7 MHz during 15 min. Reflections from the E-layer, interlayer, and two-hop reflections disappeared when the maximum of the X2.2 SF was observed.

During the X9.3 SF, the observation conditions were different. Two of the OIS paths were in the sunlit regions (Cyprus-Tory and Norilsk-Tory), while the other two—Magadan-Tory and Khabarovsk-Tory—were in the nightside sector. In Figure 12 daytime conditions over the OIS paths are shown by the thick line and nighttime conditions are shown by the thin line. The HF blackout was registered over the Cyprus-Tory path at 12:00 UT. After that, slight two-hop reflections from the *F* region appeared at 12:15 UT. After that the reflections over the Cyprus-Tory path restored gradually. Over Norilsk-Tory path the degradation of the HF signal begins at 11:58 UT from disappearance the two-hop reflections. The maximum recorded value of LOF over the path was 10 MHz at 12:03 UT. The reaction to X9.3 SF for the Khabarovsk-Tory and Magadan-Tory paths was very weak.

The bottom panel in Figure 12 shows a qualitative analysis of the amplitude characteristics of the OIS data based on the summation amplitudes method. We show data from 8 to 14 UT on the 2017 September 6. One can see a sharp decrease of the summary amplitudes over all studied OIS paths for the X2.2 SF. The severe depression of the summary amplitudes is registered over Cyprus-Tory path for the X9.3 SF with the maximum at 12:02 UT. For the other paths the response of amplitudes summation to the X9.3 SF is insignificant.

5. Conclusions

In this work, we investigated effects of the X2.2 and X9.3 SFs of 6 September 2017 on the Earth's ionosphere, GNSS-based navigation, and on HF-radio propagation.

We observed a significant impact of the SFs on the whole sunlit ionosphere. In the absolute VTEC, the first X2.2 SF caused ~3–4 TECU enhancement at middle latitudes on the dayside. The more intensive X9.3 SF produced a sudden increase of ~8–10 TECU at midlatitudes and of ~15–16 TECU enhancement at low latitudes. These latter effects lasted longer than the solar UV emission and can be explained by rather long decay of the flare emission (as shown by Qian et al., 2011) and/or by large contributions from higher altitudes (above 300 km) where the recombination is lower (Le et al., 2016).

The averaged amplitude of dTEC variations on the whole sunlit area was ~1.3 TECU for X9.3 and ~0.2 TECU for X2.2. The maximum dTEC amplitudes were recorded around subsolar regions, which is in line with previous observations. Maximums of TEC variations correspond to maximums in the UV flux. The mean values of the maximum TEC rate are 0.557 TECU/min for X9.3 and 0.071 TECU/min for X2.2. The dependence on solar zenith angle shows the maximum TEC rate in the subsolar region of ~1.3 TECU/min for X9.3 SF and 0.18 TECU/min for the X2.2 SF. This reasonably agrees with the results from the geostationary satellites which revealed ~0.24 TECU/min for X2.2 event and ~1.7 TECU/min for X9.3 event. It should be noted that dependence on solar zenith angle showed a nonzero value for TEC derivative at zero solar zenith angle, as follows from the linear interpolation.

The X9.3 SF worsened the quality of PPP in GPS and GLONASS systems for ~30 min (from 11:57 UT till ~12:25 UT). During this period of time, the GPS PPP error 3 times exceeded the background level. In terms

of the SF impact on the GNSS, surprisingly, we did not find strong effects of the X2.2 or X9.3 SFs on GNSS losses-of-lock. Based on our results, and comparing to previous works where even 4,000–12,000 sfu caused degradation of GNSS signals, nowadays SFs seem to be less threatening for the GNSS operation. The improvement in the operation quality seems to be connected with a recent increase in satellite transmitter power and in received signal strength. It is likely that in the near future the navigation systems will be more stable against the majority of SRBs.

The 6 September 2017 SFs had an impact on the HF-radiowave propagation. HF signal blackouts were recorded at Cyprus-Tory path at 09:15 UT (X2.2) and at 12:00 UT (X9.3) due to X-ray increase. The X2.2 SF also resulted in deterioration of HF radio communication quality for Norilsk-Tory, Khabarovsk-Tory, and Magadan-Tory. The lowest observable frequency demonstrated 7 MHz increase resulting in full absorption at frequencies $<$15 MHz on the dayside out of the subsolar region. During the X9.3 SF the Khabarovsk-Tory and Magadan-Tory paths were on the night side and were not under impact.

Acknowledgments
We thank the OMNIWeb Plus service (http://omniweb.gsfc.nasa.fov) for the geophysical and interplanetary data, the World Data Center (WDC) for Geomagnetism, Kyoto (http://wdc.kugi.kyoto-u.ac.jp/aedir/) for the auroral electrojet data, and Radio Solar Telescope Network (ftp://ftp.ngdc.noaa.gov/STP/space-weather/solar-data/solar-features/solar-radio) for the solar radio emission data. We acknowledge the CEDAR OpenMadrigal Services for the data of the absolute VTEC (http://cedar.openmadrigal.org). We thank the global and regional networks of GNSS receivers: IGS (Dow et al., 2009), CHAIN (Jayachandran et al., 2009), TrigNet (ftp://ftp.trignet.co.za), GEOSCIENCE AUSTRALIA (ftp://ftp.ga.gov.au/geodesy-outgoing), NOAA (ftp://www.ngs.noaa.gov/), LPIM (ftp://geoftp.ibge.gov.br/informacoes_sobre_posicionamento_geodesico/rbmc/dados), New Zealand GEONET (https://www.geonet.org.nz), Sonel (ftp://ftp.sonel.org), UNAVCO (unavco.org), and KASI (ftp://nfs.kasi.re.kr) networks for the data. We are grateful to Zhou et al. (2018) for the GAMP software code. Results on geostationary observations were obtained under Russian Science Foundation grant 17-77-20087. Results on GNSS TEC response effect were performed under Russian Science Foundation grant 17-77-20005. HF facilities from Angara Center for Common Use of scientific equipment (http://ckp-rf.ru/ckp/3056/) were operated under budgetary funding of Basic Research program II.12. Geophysical analyzes were done by EA with the support of the European Research Council (ERC, grant agreement 307998).

References

Afraimovich, E. L. (2000). GPS global detection of the ionospheric response to solar flares. *Radio Science*, *35*(N6), 1417–1424. https://doi.org/10.1029/2000RS002340

Afraimovich, E. L., Astafyeva, E. I., Oinats, A. V., Yasukevich, Y. V., & Zhivetiev, I. V. (2008). Global electron content: A new conception to track solar activity. *Annales Geophysicae*, *26*(2), 335–344. https://doi.org/10.5194/angeo-26-335-2008

Afraimovich, E. L., Demyanov, V. V., Ishin, A. B., & Smolkov, G. Y. A. (2008). Powerful radiobursts as a global and free tool for testing satellite broadband systems, including GPS-GLONASS-GALILEO. *Journal of Atmospheric and Solar - Terrestrial Physics*, *70*(15), 1985–1994. https://doi.org/10.1016/j.jastp.2008.09.008

Afraimovich, E. L., Zherebtzov, G. A., & Smolkov, G. Y. (2007). Total failure of GPS during a solar flare on December 6, 2006. *Doklady Earth Sciences*, *417*(1), 1231–1235. https://doi.org/10.1134/S1028334X07080223

Afraimovich, E. L., Astafyeva, E. I., Demyanov, V. V., Edemskiy, I. K., Gavrilyuk, N. S., Ishin, A. B., et al. (2013). Review of GPS/GLONASS studies of the ionospheric response to natural and anthropogenic processes and phenomena. *Journal of Space Weather and Space Climate*, *3*. https://doi.org/10.1051/swsc/2013049.2013

Astafyeva, E., Yasukevich, Y., Maksikov, A., & Zhivetiev, I. (2014). Geomagnetic storms, super-storms and their impact on GPS-based navigation. *Space Weather*, *12*, 508–525. https://doi.org/10.1002/2014SW001072

Berngardt, O. I., Ruohoniemi, J. M., Nishitani, N. N., Shepherd, S. G., Bristow, W. A., & Miller, E. S. (2018). Attenuation of decameter wavelength sky noise during X-ray solar flares in 2013–2017 based on the observations of midlatitude HF radars. *Journal of Atmospheric and Solar-Terrestrial Physics*, *173*, 1–13. https://doi.org/10.1016/j.jastp.2018.03.022

Cerruti, A. P., Kintner, P. M., Gary, D. E., Lanzerotti, L. J., de Paula, E. R., & Vo, H. B. (2006). Observed solar radio burst effects on GPS/Wide Area Augmentation System carrier-to-noise ratio. *Space Weather*, *4*, S10006. https://doi.org/10.1029/2006SW000254

Demyanov, V. V., Yasukevich, Y. V., Ishin, A. B., & Astafyeva, E. I. (2012). Effects of ionosphere super-bubble on GPS performance depending on the bubble orientation relative to geomagnetic field. *GPS Solutions*, *16*(N2), 181–189. https://doi.org/10.1007/s10291-011-0217-9

Demyanov, V. V., Yasyukevich, Y. V., & Jin, S. (2013). Effects of solar radio emission and ionospheric irregularities on GPS/GLONASS performance, chapter in book *Geodetic sciences—Observations, modeling and applications*, Prof. Shuanggen Jin (Ed.), P. 177–222. Rijeka: InTech. Retrieved from http://www.intechopen.com/books/geodetic-sciences-observations-modeling-and-applications/effects-of-solar-radio-emission-and-ionospheric-irregularities-on-gps-glonass-performance

Dow, J. M., Neilan, R. E., & Rizos, C. (2009). The international GNSS service in a changing landscape of Global Navigation Satellite Systems. *Journal of Geodesy*, *83*(3–4), 191–198. https://doi.org/10.1007/s00190-008-0300-3

Hocke, K. (2008). Oscillations of global mean TEC. *Journal of Geophysical Research*, *113*, A04302. https://doi.org/10.1029/2007JA012798

Hofmann-Wellenhof, B., Lichtenegger, H., & Wasle, E. (2008). *GNSS Global Navigation Satellite Systems; GPS, Glonass, Galileo & more* (p. 501). Wien, New York: Springer. https://doi.org/10.1007/978-3-211-73017-1

IRN-IS-GPS-200H-003 (2016). Global Positioning Systems directorate systems engineering & integration: interface specification IS-GPS-200. NAVSTAR GPS space segment/Navigation user segment Interface Revision H, IRN003. 28 July 2016

Jayachandran, P. T., Langley, R. B., MacDougall, J. W., Mushini, S. C., Pokhotelov, D., Hamza, A. M., et al. (2009). The Canadian High Arctic Ionospheric Network (CHAIN). *Radio Science*, *44*, RS0A03. https://doi.org/10.1029/2008RS004046

Klobuchar, J. A. (1986). Ionospheric time-delay algorithm for single-frequency GPS users. *IEEE Transactions on Aerospace and Electronics System*, *23*(3), 325–331. https://doi.org/10.1109/TAES.1987.310829

Kozyreva, O. V., Pilipenko, V. A., Zakharov, V. I., & Engebretson, M. J. (2017). GPS-TEC response to the substorm onset during April 5, 2010, magnetic storm. *GPS Solutions*, *21*(3), 927–936. https://doi.org/10.1007/s10291-016-0581-6

Kunitsyn, V., Kurbatov, G., Yasyukevich, Y., & Padokhin, A. (2015). Investigation of SBAS L1/L5 signals and their application to the ionospheric TEC studies. *IEEE Geoscience and Remote Sensing Letters*, *12*(3), 547–551. https://doi.org/10.1109/LGRS.2014.2350037

Kunitsyn, V. E., Padokhin, A. M., Kurbatov, G. A., Yasyukevich, Y. V., & Morozov, Y. V. (2016). Ionospheric TEC estimation with the signals of various geostationary navigational satellites. *GPS Solutions*, *20*(4), 877–884. https://doi.org/10.1007/s10291-015-0500-2

Le, H., Liu, L., Chen, Y., & Wan, W. (2013). Statistical analysis of ionospheric responses to solar flares in the solar cycle 23. *Journal of Geophysical Research*, *118*, 576–582. https://doi.org/10.1029/2012JA017934

Le, H., Liu, L., Ren, Z., Chen, Y., Zhang, H., & Wan, W. (2016). A modeling study of global ionospheric and thermospheric responses to extreme solar flare. *Journal of Geophysical Research*, *121*, 832–840. https://doi.org/10.1002/2015JA021930

Leonovich, L. A., Afraimovich, E. L., Romanova, E. B., & Taschilin, A. V. (2002). Estimating the contribution from different ionospheric regions to the TEC response to the solar flares using data from the international GPS network. *Annales Geophysicae*, *20*(12), 1935–1941. https://doi.org/10.5194/angeo-20-1935-2002

Leonovich, L. A., Taschilin, A. V., & Portnyagina, O. A. (2010). Dependence of the ionospheric response on the solar flare parameters based on theoretical modeling and GPS data. *Geomagnetism and Aeronomy*, *50*(2), 201–210. https://doi.org/10.1134/S0016793210020076

Liu, H., Luehr, H., Watanabe, S., Kö hler, W., & Manoj, C. (2007). Contrasting behavior of the thermosphere and ionosphere in response to the 28 October 2003 solar flare. *Journal of Geophysical Research*, *112*, A07305. https://doi.org/10.1029/2007JA012313

Liu, J.-Y., Lin, C. H., Chen, Y. I., Lin, Y. C., Fang, T. W., Chen, C. H., et al. (2006). Solar flare signatures of the ionospheric GPS total electron content. *Journal of Geophysical Research*, *111*, A05308. https://doi.org/10.1029/2005JA011306

Liu, J.-Y., Lin, C. H., Tsai, H. F., & Liou, Y. A. (2004). Ionospheric solar flare effects monitored by the ground-based GPS receivers: Theory and observations. *Journal of Geophysical Research*, *109*, A01307. https://doi.org/10.1029/2003JA009931

Liu, L., Wan, W., Chen, Y., & Le, H. (2011). Solar activity effects on the ionosphere: A brief review. *Chinese Science Bulletin*, *56*(12), 1202–1211. https://doi.org/10.1007/s11434-010-4226-9

Liu, L., Wan, W., Ning, B., & Zhang, M.-L. (2009). Climatology of the mean total electron content derived from GPS global ionospheric maps. *Journal of Geophysical Research*, *114*, A06308. https://doi.org/10.1029/2009JA014244

Mitra, A. P. (1974). *Ionospheric effects of solar flares* (p. 294). New York: Springer. https://doi.org/10.1007/978-94-010-2231-6

Podlesny, A. V., Kurkin, V. I., Medvedev, A. V., & Ratovsky, K. G. (2011). Vertical ionosphere sounding using continuous signals with linear frequency modulation, 30th URSI General Assembly and Scientific Symposium, URSIGAAS2011, 6051145. https://doi.org/10.1109/URSIGASS.2011.6051145

Qian, L., Burns, A. G., Chamberlin, P. C., & Solomon, S. C. (2011). Variability of thermosphere and ionosphere responses to solar flares. *Journal of Geophysical Research*, *116*, A10309. https://doi.org/10.1029/2011JA016777

Rideout, W., & Coster, A. (2006). Automated GPS processing for global total electron content data. *GPS Solutions*, *10*(3), 219–228. https://doi.org/10.1007/s10291-006-0029-5

Schaer, S., Beutler, G., & Rothacher, M. (1998) Mapping and predicting the ionosphere, Proceedings of the IGS AC Workshop, pp. 307–320, Darmstadt, Germany, February 9-11.

Sreeja, V., Aquino, M., de Jong, K., & Visser, H. (2014). Effect of the 24 September 2011 solar radio burst on precise point positioning service. *Space Weather*, *12*, 143–147. https://doi.org/10.1002/2013SW001011

Sripathi, S., Balachandran, N., Veenadhari, B., Singh, R., & Emperumal, K. (2013). Response of the equatorial and low-latitude ionosphere to an intense X-class solar flare (X7/2B) as observed on 09 August 2011. *Journal of Geophysical Research*, *118*, 2648–2659. https://doi.org/10.1002/jgra.50267

Tsugawa, T., Sadakane, T., Sato, J., Otsuka, Y., Ogawa, T., Shiokawa, K., & Saito, A. (2006). Summer-winter hemispheric asymmetry of sudden increase in ionospheric total electron content induced by solar flares: A role of O/N2 ratio. *Journal of Geophysical Research*, *111*, A11316. https://doi.org/10.1029/2006JA011951

Tsurutani, B. T., Judge, D. L., Guarnieri, F. L., Gangopadhyay, P., Jones, A. R., Nutall, J., et al. (2005). The October 28, 2003 extreme EUV solar flare and resultant extreme ionospheric effects: Comparison to other Halloween events and the Bastille Day event. *Geophysical Research Letters*, *32*, L03S09. https://doi.org/10.1029/2004GL021475

Tsurutani, B. T., Verkhoglyadova, O. P., Mannucci, A. J., Lakhina, G. S., Li, G., & Zank, G. P. (2009). A brief review of "solar flare effects" on the ionosphere. *Radio Science*, *44*, RS0A17. https://doi.org/10.1029/2008RS004029

Vertogradov, G. G., Sklyarevsky, M. S., Uryadov, V. P., & Valov, V. A. (2017). Oblique sounding of the ionosphere by means of an ionosonde-direction finder with chirp signal. *Radiophysics and Quantum Electronics*, *59*(11), 888–899. https://doi.org/10.1007/s11141-017-9759-1

Wan, W., Liu, L., Yuan, H., Ning, B., & Zhang, S. (2005). The GPS measured SITEC caused by the very intense solar flare on July 14, 2000. *Advances in Space Research*, *2005*(36), 2465–2469. https://doi.org/10.1016/j.asr.2004.01.027

Xiong, B., Wan, W., Ning, B., Ding, F., Hu, L., & Yu, Y. (2014). A statistic study of ionospheric solar flare activity indicator. *Space Weather*, *12*, 29–40. https://doi.org/10.1002/2013SW001000

Yasyukevich, Y. V., Voeykov, S. V., Zhivetiev, I. V., & Kosogorov, E. A. (2013). Ionospheric response to solar flares of C and M classes in January–February 2010. *Cosmic Research*, *51*(2), 114–123. https://doi.org/10.1134/S0010952513010097

Yue, X., Wan, W., Yan, L., Sun, W., Lu, L., & Schreiner, W. S. (2018). The effect of solar radio bursts on GNSS signals. *Extreme Events in Geospace, Origins, Predictability, and Consequences*, 541–554. https://doi.org/10.1016/B978-0-12-812700-1.00022-4

Yue, X., Schreiner, W. S., Kuo, Y. H., Zhao, B., Wan, W., Ren, Z., et al. (2013). The effect of solar radio bursts on the GNSS radio occultation signals. *Journal of Geophysical Research: Space Physics*, *118*, 5906–5918. https://doi.org/10.1002/jgra.50525

Zaalov, N. Y., Moskaleva, E. V., Rogov, D. D., & Zernov, N. N. (2015). Influence of X-ray and polar cap absorptions on vertical and oblique sounding ionograms on different latitudes. *Advances in Space Research*, *56*(11), 2527–2541. https://doi.org/10.1016/j.asr.2015.09.008

Zakharov, V. I., Yasyukevich, Y. V., & Titova, M. A. (2016). Effect of magnetic storms and substorms on GPS slips at high latitudes. *Cosmic Research*, *54*(1), 20–30.

Zhang, D. H., Mo, X. H., Cai, L., Zhang, W., Feng, M., Hao, Y. Q., & Xiao, Z. (2011). Impact factor for the ionospheric total electron content response to solar flare irradiation. *Journal of Geophysical Research*, *116*, A04311. https://doi.org/10.1029/2010JA016089

Zhang, D. H., & Xiao, Z. (2005). Study of ionospheric response to the 4B flare on 28 October 2003 using international GPS service network data. *Journal of Geophysical Research*, *110*, A03307. https://doi.org/10.1029/2004JA010738

Zhang, R., Liu, L., Le, H., & Chen, Y. (2017). Equatorial ionospheric electrodynamics during solar flares. *Geophysical Research Letters*, *44*, 4558–4565. https://doi.org/10.1002/2017GL073238

Zhou, F., Dong, D., Li, W., Jiang, X., Wickert, J., & Schuh, H. (2018). GAMP: An open-source software of multi-GNSS precise point positioning using undifferenced and uncombined observations. *GPS Solutions*, *22*(2), 33. https://doi.org/10.1007/s10291-018-0699-9

Erratum

In the originally published version of this article, "SEM" was written out as "scanning electron microscope" in the captions for Figures 1, 2 and 10 but should have been "solar EUV monitor." This is been corrected, and this version may be considered the authoritative version of record.